Modeling disorder in graphene

Vitor M. Pereira
Department of Physics, Boston University, 590 Commonwealth Avenue, Boston, Massachusetts 02215, USA

J. M. B. Lopes dos Santos
CFP and Departamento de Física, Faculdade de Ciências, Universidade de Porto, 4169-007 Porto, Portugal

A. H. Castro Neto
Department of Physics, Boston University, 590 Commonwealth Avenue, Boston, Massachusetts 02215, USA

(Received 17 December 2007; revised manuscript received 4 February 2008; published 7 March 2008)

We present a study of different models of local disorder in graphene. Our focus is on the main effects that vacancies (random, compensated, and uncompensated), local impurities, and substitutional impurities bring into the electronic structure of graphene. By exploring these types of disorder and their connections, we show that they introduce dramatic changes in the low energy spectrum of graphene, viz., localized zero modes, strong resonances, gap and pseudogap behaviors, and nondispersive midgap zero modes.

DOI: 10.1103/PhysRevB.77.115109 PACS number(s): 71.23.−k, 81.05.Uw, 71.55.−i

I. INTRODUCTION

Graphene is poised to become a new paradigm in solid state physics and materials science, owing to its truly bidimensional character and a host of rich and unexpected phenomena.[1–3] These have cascaded into the literature in the wake of the seminal experiments that presented a relatively easy route toward the isolation of graphene crystals.[4]

Carbon is a very interesting element, on account of its chemical versatility: It can form more compounds than any other element.[5] Its valence orbitals are known to hybridize in many different forms such as sp^1, sp^2, sp^3, etc. As a consequence, carbon can exist in many stable allotropic forms, characterized by the different relative orientations of the carbon atoms. Carbon binds through covalence and leads to the strongest chemical bonds found in nature. Common to the most interesting forms of carbon is the so-called graphene sheet, a single plane of sp^2 carbon organized in a honeycomb lattice [Fig. 1(a)]. Graphite, for instance, is made of stackings of graphene planes, nanotubes from rolled graphene sheets, and fullerenes are wrapped graphene. Yet, for many years, it was believed that graphene itself would be thermodynamically unstable. This presumption has been overturned by a series of remarkable experiments in which truly bidimensional (one atom thick) sheets of graphene have been isolated and characterized.[4] This means that studies of the two-dimensional (2D) (Dirac) electron gas can now be performed on a truly 2D crystal, as opposed to the traditional measurements made at interfaces as in metal-oxide-semiconductor field-effect transistor and other structures.[6]

The crystalline simplicity of graphene—a plane of sp^2 hybridized carbon atoms arranged in a honeycomb lattice—is deceiving. The characteristics of the honeycomb lattice make graphene a half-filled system with a DOS that vanishes linearly at the neutrality point, and an effective, low-energy quasiparticle spectrum characterized by a dispersion which is linear in momentum[7] close to the Fermi energy. These two features underlie the unconventional electronic properties of this material, whose quasiparticles behave as Dirac massless chiral electrons.[8] Consequently, many phenomena of the realm of QED find a practical realization in this solid state material. They include the minimum conductivity when the carrier density tends to zero;[9] the new half-integer quantum Hall effect (measurable up to room temperature),[9] Klein tunneling,[10] strong overcritical positron-like resonances in the Coulomb scattering cross section analogous to supercritical nuclei in QED,[11,12] the *Zitterbewegung* in confined structures;[13] anomalous Andreev reflections,[14,15] and negative refraction[16] in *p-n* junctions.

Arguably, the most interesting and promising properties from the technological point of view are its great crystalline quality, high mobility, and resilience to very high current densities,[1] the ability to tune the carrier density through a gate voltage,[4] the absence of backscattering,[17] and the fact that graphene exhibits both spin and valley degrees of freedom which might be harnessed in envisaged spintronic[18,19] or valleytronic devices.[20]

Disorder, ever present in graphene owing to its exposed surface and the substrates, is the central concern of this pa-

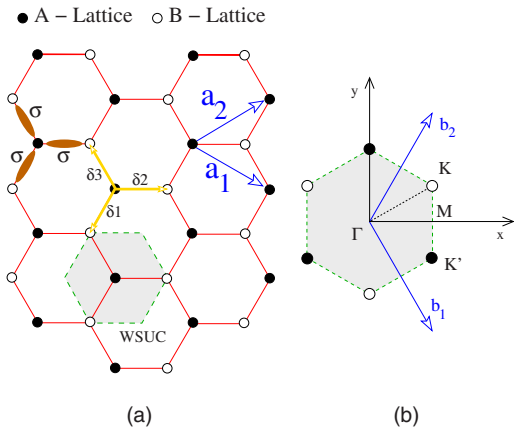

FIG. 1. (Color online) In (a), $\vec{a}_1$ and $\vec{a}_2$ are the primitive vectors that define the WS unit cell highlighted as the dashed hexagon. The lattice parameter a is $\simeq$1.4 Å. The first BZ of the associated reciprocal lattice is shown in (b), together with the points of high symmetry Γ and M and the two nonequivalent K and K'.

per. In particular, we focus on the effects of vacancies and random impurities in the electronic structure of bulk graphene. The models examined below apply to situations in which carbon atoms are extracted from the graphene plane (e.g., through irradiation[21,22]), in which adatoms and/or adsorbed species attach to the graphene plane,[23] or in which some carbon atoms are chemically substituted for other elements. They are, therefore, models of local disorder. We do not consider explicitly other sources of disorder such as rough edges or ripples,[24] or the dramatic effects of Coulomb impurities, which have been discussed elsewhere.[11,25] In this paper we expand the discussion of vacancies initiated in Ref. 26, using the same techniques, and discuss the consequences of local disorder originally presented in Ref. 27. Numerically, we resort to exact diagonalization calculations and to the recursion method.[28,29] The latter allows the calculation of the DOS and other spectral quantities for very large system sizes with disorder. In our case, the calculations below refer to honeycomb lattices with 4×10^6 carbon atoms, a size already of the order of magnitude of the real samples, if not larger for some experiments.

The paper is organized as follows. In Sec. II we present the basic electronic properties of electrons in the honeycomb lattice, mostly to introduce the notation and the details relevant for the subsequent discussions. In Sec. III we present our results regarding the different models of disorder. This section is subdivided according to the different models of disorder studied: vacancies in Secs. III A and III B, local impurities in Sec. III C, and substitutional impurities in Sec. III D. The discussion of the results is kept within each subsection and the principal findings of this paper are highlighted in Sec. IV.

II. ELECTRONS IN A HONEYCOMB LATTICE

Graphene consists of carbon atoms organized into a honeycomb lattice, bonded through covalence between two sp^2 orbitals of neighboring atoms [Fig. 1(a)]. The graphene plane is defined by the plane of the sp^2 orbitals. The saturation of the resulting σ bonding orbitals leaves an extra electron at the remaining $2p_z$ orbital per carbon atom. Ideal graphene has therefore a half-filled electronic ground state.

The Bravais lattice that underlies the translation symmetries of the honeycomb lattice is the triangular lattice, whose primitive vectors $\vec{a}_1$ and $\vec{a}_2$ are depicted in Fig. 1(a). One of the consequences is the existence of two atoms per unit cell that define two sublattices (A and B in the figure): Indeed, the honeycomb lattice can be thought as two interpenetrating triangular lattices. This bipartite nature of the crystal lattice, added to the half-filled band, imposes an important particle-hole symmetry, as will be discussed later.

The electronic structure of graphene can be captured within a tight-binding approach, in which the electrons are allowed to hop between immediate neighbors with hopping integral $t\simeq2.7$ eV, and also between next-nearest neighbors with an additional hopping t',

$$H=-t\sum_{\langle i,j\rangle}c_i^\dagger c_j-t'\sum_{\langle\langle i,j\rangle\rangle}c_i^\dagger c_j+\text{H.c.} \tag{1}$$

The presence of the second term introduces an asymmetry between the valence and conduction bands, thus violating

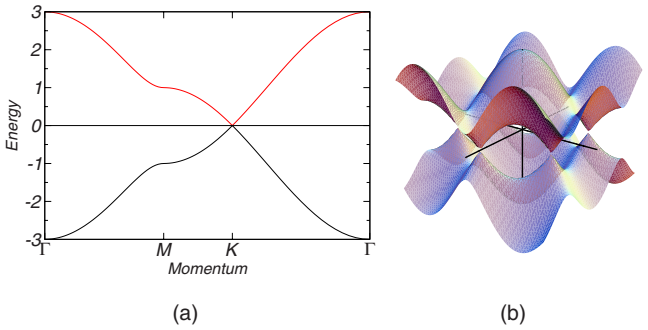

FIG. 2. (Color online) (a) Band structure along the symmetry directions in the reciprocal BZ of the honeycomb lattice. (b) Band structure of graphene ($t'=0$) with the two bands touching at the K and K' points of the BZ.

particle-hole symmetry. To emphasize the two sublattice structure of the honeycomb, we can write the Hamiltonian as

$$H=-t\sum_{i\in A,\delta}a_i^\dagger b_{i+\delta}-t\sum_{i\in B,\delta}b_i^\dagger a_{i+\delta}-t'\sum_{i\in A,\Delta}a_i^\dagger a_{i+\Delta}-t'\sum_{i\in B,\Delta}b_i^\dagger b_{i+\Delta}, \tag{2}$$

with operators a_i and b_i pertaining to sublattices A and B, respectively. The vectors $\vec{\delta}$ connect atom i to its immediate neighbors, whereas the $\vec{\Delta}$ connect atom i to its six second neighbors. Fourier transforming Eq. (2) and introducing a spinor notation for the sublattice amplitudes lead to

$$H=\sum_k\Psi_k^\dagger\begin{pmatrix}\epsilon_2(k) & \epsilon_1(k)\\ \epsilon_1(k)^* & \epsilon_2(k)\end{pmatrix}\Psi_k \quad \text{with } \Psi_k=\begin{pmatrix}a_k\\ b_k\end{pmatrix}. \tag{3}$$

Since the spin degree of freedom does not play a role in our discussion other than through a degeneracy factor, it will been omitted, for simplicity. The functions $\epsilon_1(k)$ and $\epsilon_2(k)$ read

$$\epsilon_1(k)=-t\sum_{\vec{\delta}}e^{-i\vec{\delta}\cdot\vec{k}},\quad \epsilon_2(k)=-t'\sum_{\vec{\Delta}}e^{-i\vec{\Delta}\cdot\vec{k}}, \tag{4}$$

$$\epsilon_2(k)=-2t'\cos(\sqrt{3}k_ya)-4t'\cos\left(\frac{\sqrt{3}}{2}k_ya\right)\cos\left(\frac{3}{2}k_xa\right),$$

$$|\epsilon_1(k)|^2=3t^2+2t^2\cos(\sqrt{3}k_ya)+4t^2\cos\left(\frac{\sqrt{3}}{2}k_ya\right)\cos\left(\frac{3}{2}k_xa\right), \tag{5}$$

where $\epsilon_2(k)$ alone is the dispersion relation of a triangular lattice and yield, after diagonalization of Eq. (3), the dispersion relations for graphene,

$$E_\pm(k)=\epsilon_2(k)\pm|t|\sqrt{3-\frac{\epsilon_2(k)}{t'}}. \tag{6}$$

The two bands $E_\pm(k)$ are represented in Fig. 2(b) in the domain $k_{x,y}\in[-\pi,\pi]$. This unusual band structure makes graphene very peculiar with valence and conduction bands

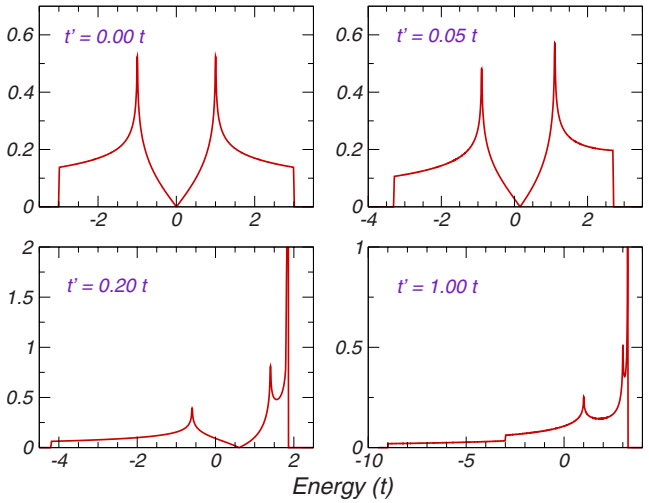

FIG. 3. (Color online) DOS associated with Eq. (6) for different values of the next-nearest-neighbor hopping t'.

touching at the Fermi energy, at a set of points at the edge of the first Brillouin zone, equivalent to the points K and K' by suitable reciprocal lattice translations. Its low energy physics is dictated by the dispersion around those two nonequivalent points, which turns out to be linear in k. In fact, expanding Eq. (5) around either

$$K = \frac{4\pi}{3\sqrt{3}a}\left(\frac{\sqrt{3}}{2}, \frac{1}{2}\right) \text{ or } K' = \frac{4\pi}{3\sqrt{3}a}\left(\frac{\sqrt{3}}{2}, -\frac{1}{2}\right), \tag{7}$$

one gets the so-called $\vec{K}\cdot\vec{p}$ *effective* band structure,[7]

$$E(\vec{K}+\vec{q}) = -3t' \pm v_F|\vec{q}| + \mathcal{O}(q^2), \tag{8}$$

with a Fermi velocity v_F ($\hbar v_F \equiv v_F = 3ta/2$, and we take units in which $\hbar = 1$ and $t = 1$). When $t' = 0$, the dispersion is purely conical, as in a relativistic electron in 2D. For this reason, the two cones tipped at K and K' are known as Dirac cones. The low-energy, continuum limit of Eq. (2) is given by

$$H = v_F \int d^2\boldsymbol{r}\,\psi^\dagger(\boldsymbol{r})\vec{\sigma}\cdot\vec{p}\,\psi(\boldsymbol{r}), \tag{9}$$

where $\psi(\boldsymbol{r})$ is a two-dimensional spinor obeying the Dirac equation in two dimensions.[30]

Some quantitative aspects of graphene's band structure [Eq. (6)] are plotted in Figs. 2 and 3 In Fig. 2(a), the band dispersion is plotted along the symmetry directions of the Brillouin zone (BZ) indicated in Fig. 1(b), and in Fig. 3, the DOS for different values of the nearest-neighbor hopping t' are plotted. Focusing on the particle-hole symmetric case ($t = 0$), it is clear that, besides the marked van Hove singularities at $E = \pm t$, the most important feature is the linear vanishing of the DOS at the Fermi level, a fact that is at the origin of many transport anomalies in this material.[3,31]

Particle-hole symmetry in this problem arises from the bipartite nature of the honeycomb lattice and is a general property of systems whose underlying crystal lattice has this nature. When we have a bipartite lattice, the basis vectors of the Hilbert space can be ordered so that, for any ket, $|\varphi\rangle$, the amplitudes in sublattice A come first. For example, if $\{\phi_A^1, \phi_A^2, \ldots, \phi_A^N\}$ are the Wannier functions for the orbitals in sublattice A and $\{\phi_B^1, \phi_B^2, \ldots, \phi_B^N\}$ the ones in sublattice B, then our ordered basis could be $\{\phi_A^1, \ldots, \phi_A^N; \phi_B^1, \ldots, \phi_B^N\}$. If the Hamiltonian includes hopping only between nearest neighbors, this means that it only promotes itinerancy between different sublattices. The stationary Schrödinger equation then reads, in matrix block form in the ordered basis,

$$\begin{pmatrix} 0 & h_{AB} \\ h_{AB}^\dagger & 0 \end{pmatrix}\begin{pmatrix} \varphi_A \\ \varphi_B \end{pmatrix} = E\begin{pmatrix} \varphi_A \\ \varphi_B \end{pmatrix}. \tag{10}$$

Expanding, we get

$$\begin{aligned} h_{AB}\varphi_B &= E\varphi_A \\ h_{AB}^\dagger\varphi_A &= E\varphi_B \end{aligned} \Rightarrow (h_{AB}^\dagger h_{AB})\varphi_B = E^2\varphi_B, \tag{11}$$

and therefore, if E is an eigenstate, so is $-E$. For a half-filled system, the elementary excitations around the Fermi sea can be thought, as usual, as particle-hole pairs. Since in that case $E_F = 0$, particles and holes have symmetric dispersions. This is completely analogous to the situation found in simple semiconductors or semimetals, although matters are slightly more complicated in graphene because there are two degenerate points, K and K', in the BZ. Thus, there will be two families of particle and hole excitations: one associated with the Dirac cone at K and the other with the cone at K', like in a multivalley semiconductor.

III. LOCAL DISORDER IN GRAPHENE

Disorder is present in any real material, graphene being no exception. In fact, true long-range order in two dimensions implies a broken continuous symmetry (translation), which violates the Hohenberg–Mermin–Wagner theorem.[32,33] So, by this reason alone, defects must be present in graphene and, in a sense, as paradoxical as it might sound, are presumably at the basis of its thermodynamic stability.

However, the study of disorder effects on graphene is motivated by more extraordinary experimental results. One of them is the study undertaken in Refs. 21 and 22 in which highly oriented pyrolytic graphite samples were irradiated via high-energy proton beams. As a result, the experiments revealed that the samples acquired a magnetic moment, displaying long-range ferromagnetic order up to temperatures much above 300 K. This triggered enormous interest since the technological possibilities arising from organic magnets are many and varied. Furthermore, carbon, being the most covalent of the elements, has a strong tendency to saturate its shell in its allotropes and is somehow the antithesis of magnetism. Besides the moment formation, it was found that the magnitude of the saturation moment registered in hysteresis curves was progressively increased with successive irradiations. This is strong evidence that the defects induced by the proton beam are playing a major role in this magnetism. In this context, the study of defects and disorder in graphene gains a significant pertinence.

In the following paragraphs, we will unveil some details and peculiarities that emerge from different models of disor-

der applied to free electrons in the honeycomb lattice.

A. Vacancies

Vacancies are one of the defects more likely to be induced in the graphene structure by proton irradiation. A vacancy is simply the absence of an atom at a given site. When an atom is removed, two scenarios are possible: either the disrupted bonds remain as dangling bonds or the structure undergoes a bond reconstruction in the vicinity of the vacancy, with several possible outcomes.[34] In either case, a slight local distortion of the lattice is expected. In the following discussion, however, it is assumed that, as first approximation, the creation of a vacancy has the sole effect of removing the π_z orbital at a lattice point, together with its conduction band electron. In this sense, the physics of the conduction band electrons is still described by the Hamiltonian (1), where now the hopping to the vacancy sites is *forbidden*.

1. Vacancies, uncompensated lattices, and a theorem

Vacancies have an interesting consequence when $t'=0$. If the distribution of vacant sites is uneven between the two sublattices, zero energy modes will necessarily appear. This follows from a theorem in linear algebra[35] and can be seen as follows. Assume, very generally, that we have a bipartite lattice, with sublattices A and B (It can be any bipartite lattice like the square or honeycomb lattices in two dimensions, cubic in three dimensions, etc.), and that the number of orbitals and/or sites in A (B) is N_A (N_B). Just as we did before, the basis vectors of the Hilbert space can always be ordered so that any ket $|\Psi\rangle$ has the amplitudes on sublattice A appearing first, followed by the amplitudes on sublattice B,

$$|\Psi\rangle = (\varphi_A, \varphi_B) = (\phi_A^1, \phi_A^2, \ldots, \phi_A^{N_A}; \phi_B^1, \phi_B^2, \ldots, \phi_B^{N_B}). \tag{12}$$

We now consider a Hamiltonian containing only nearest-neighbor hopping, plus some local energy (ϵ_A, ϵ_B) on each sublattice. The corresponding stationary Schrödinger equation will then be (in matrix block form that respects the ordering of the basis)

$$\mathcal{H}|\Psi\rangle = E|\Psi\rangle \mapsto \begin{pmatrix} \epsilon_A \mathbb{1}_{N_A} & h_{AB} \\ h_{AB}^\dagger & \epsilon_B \mathbb{1}_{N_B} \end{pmatrix} \begin{pmatrix} \varphi_A \\ \varphi_B \end{pmatrix} = E \begin{pmatrix} \varphi_A \\ \varphi_B \end{pmatrix}, \tag{13}$$

where $\mathbb{1}_M$ is the $M \times M$ identity matrix, h_{AB} a $N_A \times N_B$ matrix, and φ_A (φ_B) a vector in a subspace of dimension N_A (N_B).

To analyze the spectrum, we note that

$$h\varphi_B = (E - \varepsilon_A)\varphi_A,$$

$$h^\dagger \varphi_A = (E - \varepsilon_B)\varphi_B, \tag{14}$$

which, from cross substitution, implies that

$$h^\dagger h \varphi_B = (E - \varepsilon_A)(E - \varepsilon_B)\varphi_B. \tag{15}$$

If we call λ^2 to the (non-negative) eigenvalues of $h^\dagger h$, the spectrum of $\mathcal{H}$ is then

$$E = \frac{\varepsilon_A + \varepsilon_B}{2} \pm \sqrt{\left(\frac{\varepsilon_A - \varepsilon_B}{2}\right) + \lambda^2}. \tag{16}$$

The symmetry about $(\varepsilon_A + \varepsilon_B)/2$ simply reflects the particle-hole symmetry.

States of a *peculiar* nature should appear when the number of sites in each sublattice is different. Without any loss of generality, we take $N_A > N_B$. Since the block h_{AB} in Eq. (13) is a linear application from a vector space having $\dim(A) = N_A$ onto a vector space B with $\dim(B) = N_B$, it follows from basic linear algebra that

(a) $\mathrm{rank}(h_{AB}) = \mathrm{rank}(h_{AB}^\dagger) = N_B$;

(b) $h_{AB}\varphi_B = 0$ has no solutions other than the trivial one; and

(c) $h_{AB}^\dagger \varphi_A = 0$ has nontrivial solutions that we call φ_A^0.

From the rank-nullity theorem,

$$\mathrm{rank}(h_{AB}^\dagger) + \mathrm{nullity}(h_{AB}^\dagger) = N_A, \tag{17}$$

and hence the null space of $h_{AB}^\dagger$ has dimension: $\mathrm{nullity}(h_{AB}^\dagger) = N_A - N_B$. Consequently, there are states of the form

$$|\Psi^0\rangle = (\varphi_A^0; 0),$$

in which φ_A^0 satisfies $h_{AB}^\dagger \varphi_A^0 = 0$ that are eigenstates of $\mathcal{H}$ with eigenvalue ε_A,

$$\mathcal{H}|\Psi^0\rangle = E|\Psi\rangle \Leftrightarrow \begin{cases} h0 = (\varepsilon_A - \varepsilon_A)\varphi_A \\ h^\dagger \varphi_A^0 = (\varepsilon_A - \varepsilon_B)0. \end{cases} \tag{18}$$

Furthermore, since $\mathrm{nullity}(h_{AB}^\dagger) = N_A - N_B$ implies the existence of $N_A - N_B$ linearly independent φ_A^0, this eigenstate has a degeneracy of $N_A - N_B$. It should be stressed that a state of the form $(\varphi_A; 0)$ has only amplitude in the A sublattice. Therefore, the following theorem is established: Whenever the two sublattices are not balanced with respect to their number of atoms, there will appear $N_A - N_B$ states with energy $E = \varepsilon_A$, all linearly independent and localized only on the *majority* sublattice. In addition, one can modify sublattice B in any way (remove more sites, for instance) that these zero modes will remain undisturbed.

We remark that in the above, the details of the hopping matrix h_{AB} were not specified and need not be. The result holds in general, provided that the hopping induces transitions between different sublattices only, and that the diagonal energies are constant (diagonal disorder is excluded).

2. Zero modes

The case with $\varepsilon_A = \varepsilon_B = 0$ is of obvious relevance for us since our model for pristine graphene does not include any local potentials. In this situation, the above results imply that introducing a vacancy in an otherwise perfect lattice immediately creates a zero energy mode. Now, this is important because those states are created precisely at the Fermi level, and have this peculiar topological localization determining that they should live in just one of the lattices.

Even more interestingly, it is possible to obtain the exact analytical wave function associated with the zero mode induced by a single vacancy in a honeycomb lattice. This was

done by the authors and collaborators in Ref. 26 and will not be repeated here. We only mention that the wave function can be constructed by an appropriate matching of the zero modes of two semi-infinite and complementary ribbons of graphene, and that, in the continuum limit, the wave function of the zero mode introduced by one vacancy has the form[26]

$$\Psi(x,y) \simeq \frac{e^{iK'\cdot r}}{x+iy} + \frac{e^{iK\cdot r}}{x-iy}. \tag{19}$$

The important point is that the amplitude of this state decays with the distance to the vacancy as $\sim 1/r$ and thus has a quasilocalized character, although strictly not normalizable, and such quasilocalized state appears exactly at the Fermi level.

Should another vacancy be introduced in the same sublattice, another zero mode will appear. However, the nature of the two zero modes will depend whether the vacancies are close or distant. In the latter case, the hybridization between the two modes should be small on account of the $1/r$ decay, and we can expect two states of form (19) about each vacancy site. Of course, significant effects in the thermodynamic limit can only arise with a finite concentration of vacancies, and for such analysis, we undertook the numerical calculations described next.

3. Numerical results: Single vacancy

The first calculation is the numerical verification of the exact analytical result for the localized state in Eq. (19). For that, we consider the tight-binding Hamiltonian (1) and calculate numerically, via exact diagonalization, the full spectrum and eigenstates in the presence of a single vacancy. For some typical results, we turn our attention to Fig. 4. There, we plot a real-space representation of some selected wave functions. This has been done by drawing a circle at each lattice site, whose radius is proportional to the wave function amplitude at that site, and whose color (red/blue) reflects the sign $(+/-)$ of the amplitude at each site. Thus, bigger circles mean higher amplitudes. In the first panel [Fig. 4(a)], we are showing the eigenstate with lowest, yet nonzero, absolute energy. It is visible that the wave function associated with such state spreads uniformly across the totality of the system such as a plane wave. In the second panel [Fig. 4(b)], we draw the wave function of the state $E=0$, which corresponds to Eq. (19). The state is clearly decaying as the distance to the central vacancy increases. In addition, the state exhibits the full C_3 point symmetry about the vacant site, just as expected. This picture provides a snapshot of the lattice version[26] of Eq. (19). Since only one vacancy was introduced, the state shown in Fig. 4(b) is the only zero mode present.

When particle-hole symmetry is disturbed by a nonzero t', we still find states having this quasilocalized nature, where the wave function amplitude is still quite concentrated about the vacancy. Two examples are shown in panels Figs. 4(b) and 4(c). They are two eigenstates with neighboring energy calculated for the same system. An important difference occurs here, in that, unlike the case $t'=0$ where only one localized state appears, the particle-hole asymmetric case

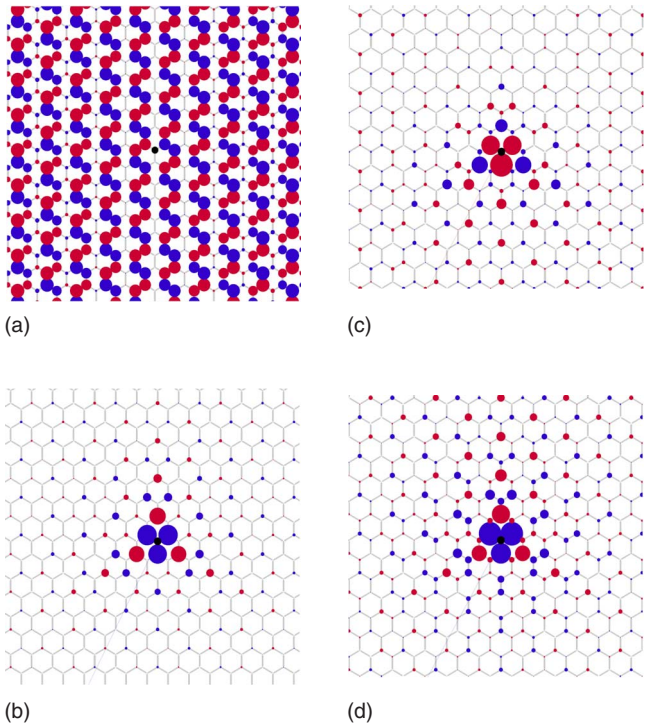

FIG. 4. (Color online) Selected eigenstates in a graphene sheet with 80^2 atoms containing a single impurity at the center (black dot). Only the region near the vacancy is shown. (a) The eigenstate with energy closest, but different, to zero. (b) The eigenstate with $E=0$. (c) and (d) show the presence of two quasilocalized eigenstates even with $t=0.2t$.

opens the possibility for more than one of such states.

This fact can be seen more transparently through the IPR of the eigenstates. With such purpose in mind, the IPR

$$\mathcal{P}(E_n) = \sum_i |\Psi_n(r_i)|^4$$

was calculated across the band in both the $t'=0$ and $t'\neq 0$ cases, with a single central vacancy. Typical results are shown in Fig. 5. From Fig. 5(a), we do confirm that, when $t'=0$, the presence of a vacancy introduces a localized state at $E=0$, which is reflected both by the enhanced IPR there, and by the sharply peaked local density of states (LDOS) calculated at the vicinity of the vacancy site. Although not shown in this figure, the amplitude of the peak in the LDOS at $E=0$, $\rho_i(0)$, decays as the distance between $\vec{R}_i$ and the vacancy increases, in total consistence with the analytical picture. When next-nearest-neighbor hopping is included, we also confirm the appearance of states with a considerably enhanced IPR. Not only that, but, instead of one, we do observe a set of states with IPR much larger than the average for the remainder of the band. The LDOS is also enhanced near these energies, although the effect appears as a resonance on account of the finite DOS, in contrast with the sharp peak in the previous, particle-hole symmetric, case.

A more definite and quantitative analysis is provided by the results in the subsequent panel [Fig. 5(b)]. Here, we present the dependence of $\mathcal{P}(E)$ on the number of carbon

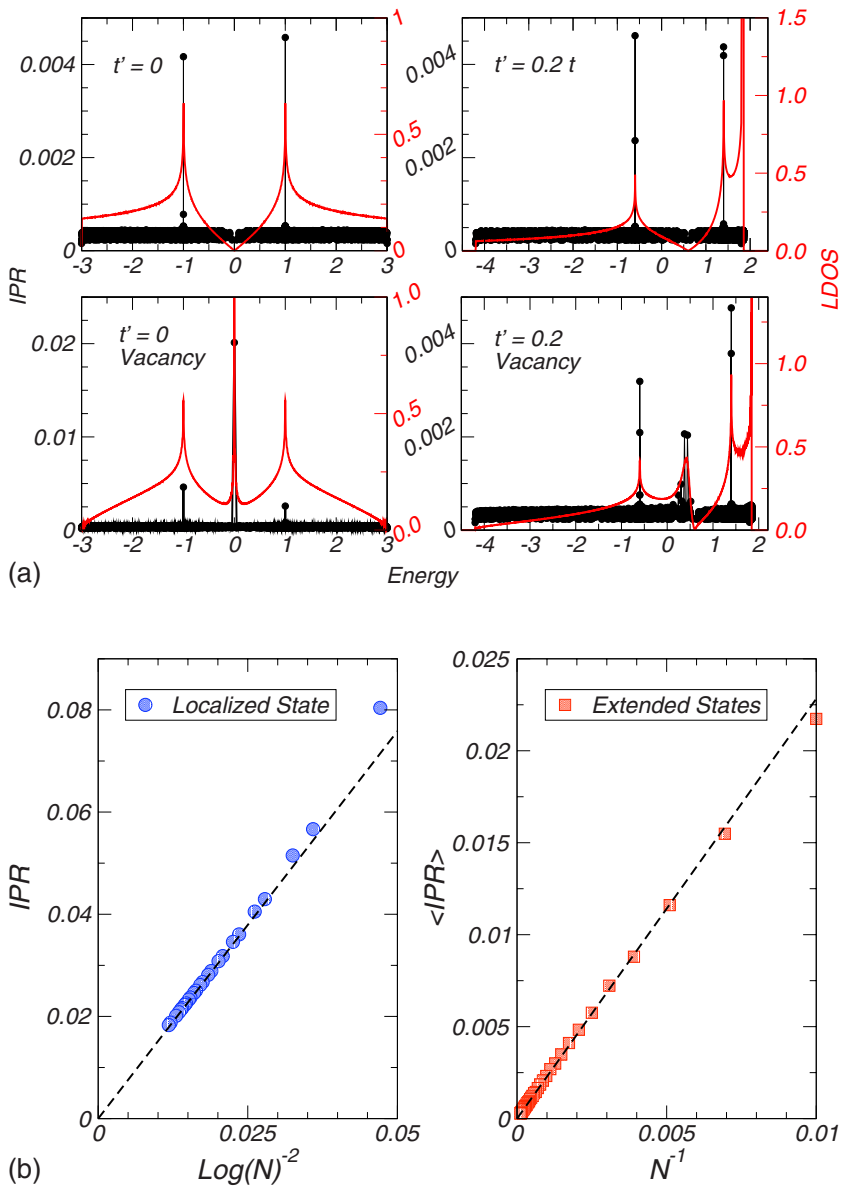

FIG. 5. (Color online) IPR and LDOS calculated at one site closest to the vacancy. In panel (a), we have results for the IPR with $t'=0$ and $t'\neq 0$ without any vacancy (top row) and with a single vacancy (bottom) for comparison. In panel (b), we show the dependence of the IPR of the zero mode, $\mathcal{P}(E=0)$, with the system size N (left), and also $\langle \mathcal{P}(E) \rangle$ versus N for the remainder (extended) states (right). Dashed lines are guides for the eye.

atoms in the system N. To understand the differences, we recall that the IPR for extended states should scale as

$$\mathcal{P}(E) \sim \frac{1}{N}. \tag{20}$$

However, for the zero mode (it should be obvious that when the term *zero mode* is employed, we are referring to the case with $t'=0$), we face an interesting circumstance. Remember that wave function (19) is not normalizable. So, strictly speaking, the state is not localized and hence the designation *quasilocalized* that we have adopted above. The consequence of this is that the normalization constant for $\Psi(x,y)$ depends on the system size,

$$\sum_i^N |\Psi(x,y)|^2 \sim \log(\sqrt{N}) \sim \log(N). \tag{21}$$

This, in turn, has an effect on the IPR because $\mathcal{P}(E)$ is defined in terms of normalized wave functions,

$$\mathcal{P}(0) = \frac{1}{\log(N)^2} \sum_i^N |\Psi(x,y)|^4 \sim \frac{1}{\log(N)^2}. \tag{22}$$

This scaling of the IPR with N is precisely the one obtained numerically in Fig. 5(b) (left) for the zero mode and is just another way of confirming the $1/r$ decay of this wave function.

4. Numerical results: Finite concentration of vacancies

Unlike the single vacancy case, the dilution of the honeycomb via the introduction of a finite concentration of vacancies is not solvable using the analytical expedients employed in Ref. 26, and numerical calculations become essential in this case. Our procedure consists in diluting the honeycomb lattice with a constant concentration of vacancies, which we call x ($x=N_{\mathrm{vac}}/N$). The diluted sites are chosen at random and the global DOS, averaged over several vacancy configurations, is calculated afterward. This is clearly a disordered problem, and we employ the recursive method allowing us to obtain the DOS for systems with 2000^2 sites (which is already of the order of magnitude of the number of atoms in real mesoscopic samples of graphene studied experimentally). Some results are summarized in Fig. 6. One of the effects of this disorder is, as always, the softening of the van Hove singularities (not shown). However, the most significant changes occur in the vicinity of the Fermi level [Fig. 6(a)]. In the presence of electron-hole symmetry ($t'=0$), the inclusion of vacancies brings an increase of spectral weight to the surroundings of the Dirac point, leading to a DOS whose behavior for $E\approx 0$ mostly resembles the results obtained elsewhere within CPA.[31] Indeed, for higher dilutions, there is a flattening of the DOS around the center of the band just as in CPA. The most important feature, however, is the emergence of a sharp peak at the Fermi level, superimposed upon the flat portion of the DOS (apart from the peak, the DOS flattens out in this neighborhood as x is increased past the 5% shown here). The breaking of the particle-hole symmetry by a finite t' results in the broadening of the peak at the Fermi energy, and the displacement of its position by an amount of the order of t'. All these effects take place close to the Fermi energy. At higher energies, the only deviations from the DOS of a clean system are the softening of the van Hove singularities and the development of Lifshitz tails (not shown) at the band edge, both induced by the increasing disorder caused by the random dilution. The onset of this high energy regime, where the profile of the DOS is essentially unperturbed by the presence of vacancies, is determined by $\epsilon\approx v_F/l$, with $l\sim n_{\mathrm{imp}}^{-1/2}$ being essentially the average distance between impurities.

To address the degree of localization for the states near the Fermi level, the IPR was calculated again via exact diagonalization on smaller systems. Results for different values of t' are shown in Fig. 6(b) for random dilution at 0.5%. One observes first that $\mathcal{P}(E)\sim 3/N$ for all energies but the Fermi level neighborhood, as expected for states extended up to the length scale of the system sizes used in the numerics. Second, the IPR becomes significant exactly in the same energy range where the DOS exhibits the vacancy-induced anomalies discussed above. Clearly, the farther the system is driven from the particle-hole symmetric case, the weaker the localization effect, as illustrated by the results obtained with $t'=0.2t$. To this respect, it is worth mentioning that the magnitude of the strongest peaks in $\mathcal{P}(E)$ at $t'=0$ and $t'=0.1t$ is equal to the magnitude of the IPR calculated above for a single impurity problem. Such behavior of the IPR indicates the existence of quasilocalized states at the center of the resonance, induced by the presence of the vacancies. For higher doping strengths, the enhancement of $\mathcal{P}(E)$ is weaker in the regions where the DOS becomes flat. This means that

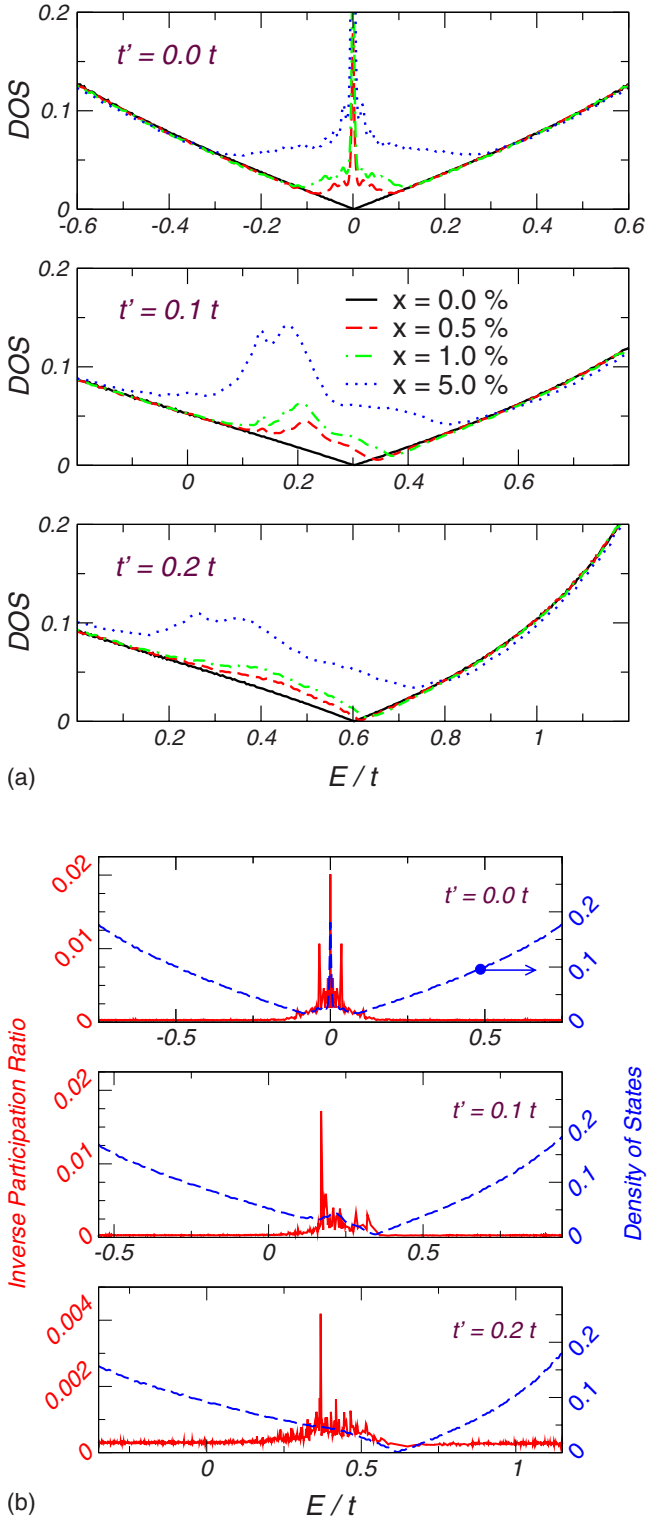

FIG. 6. (Color online) IPR and DOS for the diluted honeycomb lattice. (a) DOS for selected concentrations x and different values of t'. (b) IPR for selected values of t' using a concentration $x=0.5\%$. For comparison, the corresponding DOS is also plotted in each case. The concentration of vacancies is x, and only the vicinity of the Fermi level is shown.

only the states in the closest vicinity of the Dirac point have a localized character, which is consistent with the fact that our results for the averaged DOS qualitatively agree with CPA in the low-energy region, except closer to $E=0$, where we find the peak absent in the CPA description. Notice that, although our final DOS is always averaged over disorder configurations, it is exact for each configuration, and therefore includes all possible scattering and interference processes between electron wave and the scattering centers, which appear to be crucial at the Dirac point. As discussed in Ref. 36, many of these processes that are not captured within CPA become relevant in a narrow vicinity of the Dirac point, rendering that approximation less justifiable.

In summary, in this section, we saw that a single vacancy introduces a quasilocalized zero mode. Its presence is ensured by the uncompensation between the number of orbitals in the two sublattices, and a theorem from linear algebra. The presence of this mode translates in the appearance of a peak in the LDOS near the vacancy, and in an enhanced IPR for this state. When we go from one to a macroscopic number of vacancies, we saw that both the peak and the enhancement of the IPR persist in the global DOS at E_F.

B. Selective dilution

It is important to recall that the results of the previous section pertain to lattices that were randomly diluted. During such process, we expect the number of vacancies in sublattice A to be equal to the number of vacancies in sublattice B, on average. Strictly speaking, since our original lattices are always chosen with $N_A=N_B$, the fluctuations on the degree of uncompensation, N_A-N_B, should scale as $1/\sqrt{N}$ thus vanishing in the thermodynamic limit. Because of this, in principle, we would expect the lattices used above to be reasonably compensated. However, the theorem in Sec. III A 1 only guarantees the presence of zero modes when the lattice is uncompensated. It turns out that, notwithstanding our utilization of rather large system sizes, such $\sqrt{N}$ fluctuations are still significant and the lattices were indeed slightly uncompensated.

This clearly begs the clarification of the origin of the zero modes in the cases with finite densities of vacancies. Do they appear only through these fluctuations in the degree of sublattice compensation, or can we have zero modes even with full compensation? To try to elucidate this, we developed a controlled approach to this issue in the following. From now on, we consider only the particle-hole symmetric situation ($t'=0$).

1. Complete uncompensation

We have studied the DOS for systems in which only one of the sublattices was randomly diluted, with a finite concentration of vacancies. In this case, the system has precisely a number of zero modes that equals the number of vacancies. Starting from a clean lattice with $N=N_A+N_B$ sites, the latter corresponds to $N_v=Nx$. We should thus expect a $\delta(E)$ peak contributing to the global DOS, with an associated spectral weight w_δ that coincides with the fraction of zero modes,

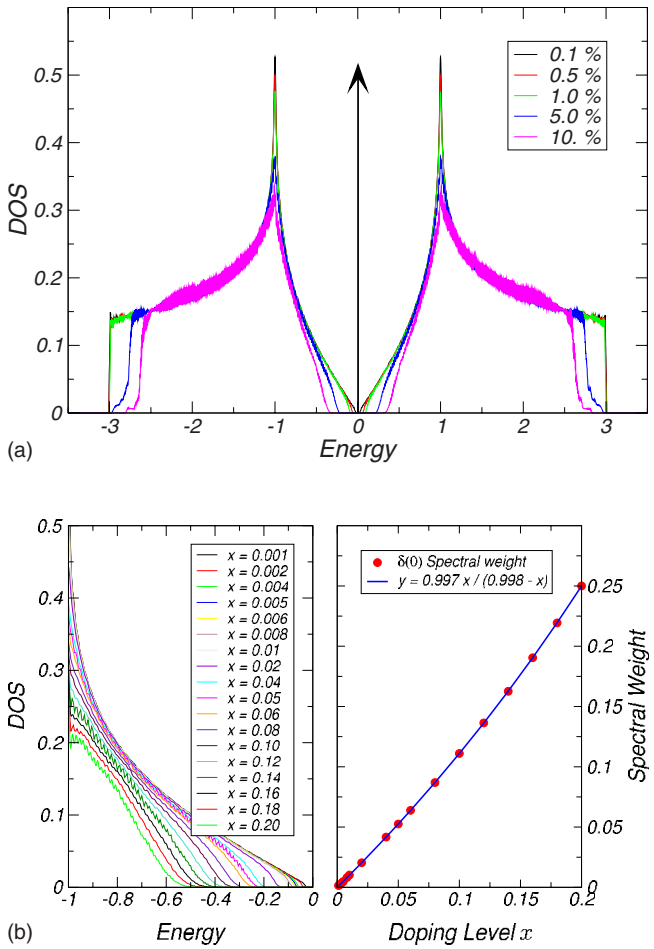

FIG. 7. (Color online) Dilution of just one sublattice of the honeycomb. (a) DOS for different dilution strengths, diluting only sublattice A. (b) On the left panel, we show a detail of the DOS and the evolution of the gap with vacancy concentrations. On the right panel, we plot the dependence of the missing spectral weight on the band ($=1-w_\delta$) with x (circles). The continuous line is the best fit using $f(x)=ax/(b-x)$ to the data represented by the circles. The coefficients yielding the best fit are $a=0.997$ and $b=0.998$, thus agreeing with the expected result [Eq. (23)].

$$w_\delta(x) = \frac{Nx}{N(1-x)} = \frac{x}{1-x}. \tag{23}$$

Since the total spectral weight is normalized to 1, the spectral weight at $E=0$ has to be transferred from the states in the band. In Fig. 7, we show what is happening. As seen in Fig. 7(a), the selective dilution promotes the appearance of a gap in the DOS, whose magnitude increases with the amount of dilution. At the center of the gap, we can only see an enormous peak (not visible in the range used) staying precisely at $E=0$, corroborating our expectations regarding the Dirac delta in the DOS. However, since it appears exactly at $E=0$, we cannot resolve numerically its associated spectral weight. To obtain such spectral weight, we calculated the spectral weight loss in the remainder of the band. The result and its variation with the amount of dilution x are displayed in the right-most frame of Fig. 7(b). A nonlinear fit to the data

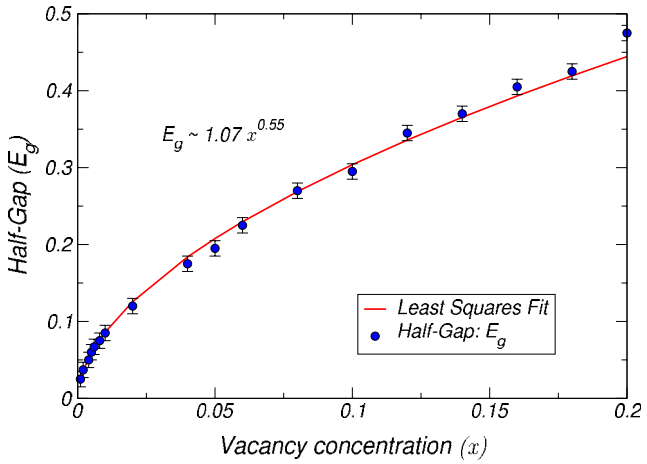

FIG. 8. (Color online) The gap estimated from the numerical curves in Fig. 7 is plotted against the vacancy concentration x. The continuous line is a least squares fit to $f(x)=ax^b$.

reveals that the dependence expected from Eq. (23) is indeed verified by the accord between the fitted curve in Fig. 7(b) and Eq. (23).

As Fig. 7 shows, the spectral weight is transferred almost entirely from the low-energy region near E_F and from the high-energy regions at the band edges. This depletion near $E=0$ introduces the gap $2E_g$. A gap implies the existence of a new energy scale in the problem. Since the hopping t is the only energy scale in the Hamiltonian, such new scale has to come from the concentration of vacancies. By dimensional analysis, such scale is dictated essentially by the average distance between vacancies (l),

$$\epsilon \sim \frac{v_F}{l} \sim n_{\text{vacancies}}^{1/2} \sim \sqrt{x} \quad (\hbar = 1). \tag{24}$$

When the magnitude of the gap found numerically is plotted against x, we arrive at the curve of Fig. 8. The least squares fit shown superimposed onto the numerical circles confirms this assumption, and we arrive at a quite interesting situation, of having a half-filled, particle-hole symmetric and gapped system, with a finite concentration of (presumably quasilocalized) zero modes at the midgap point.

2. Controlled uncompensation

We now turn to a more controlled approach to the dilution and uncompensation. For that, we introduce an additional parameter η that measures the degree of uncompensation. As before, we want to study finite concentrations of vacancies. This is determined by x in such a way that the number of vacancies in a lattice with N sites will be $N_v=Nx$. However, now, the number of vacancies in each sublattice is determined by

$$N_v^A = \frac{1}{2}Nx(1+\eta)$$

$$N_v^B = \frac{1}{2}Nx(1-\eta), \tag{25}$$

with $0 \leqslant \eta \leqslant 1$. Therefore, the parameter η permits an interpolation between completely uncompensated dilution ($\eta=1$) and totally compensated dilution ($\eta=0$). Let us look directly at the results for the DOS, calculated at different x and η and plotted in Fig. 9.

At any concentration x, the following sequence of events unfolds as η decreases from 1 to 0: (i) There is a perfectly

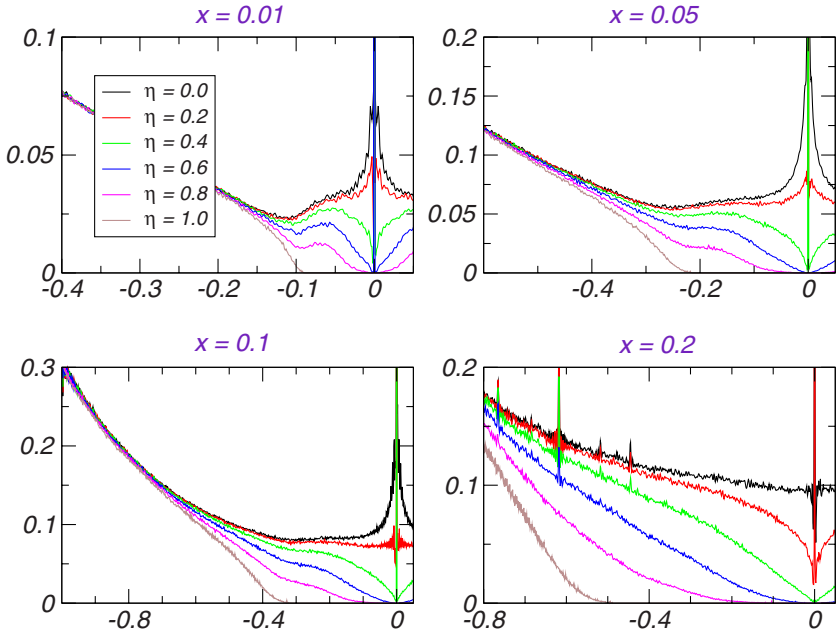

FIG. 9. (Color online) DOS for the honeycomb lattice using the controlled selective dilution discussed in the text, calculated for different concentrations of vacancies x and several degrees of uncompensation η. Only the low-energy region close to the Dirac point is shown.

defined gap in the limit $\eta=1.0$ discussed above; (ii) for $\eta \lesssim 1$, a small hump develops at the same energy scale of the previous gap; (iii) although the gap seems to disappear, it is clearly visible that when $\eta \lesssim 1$, the DOS decays to zero after the hump in a pseudogaplike manner and is zero at $E=0$; (iv) decreasing further η toward complete compensation (say, for $\eta=0.6$ and 0.4), this behavior persists, being visible that the DOS drops to zero at $E=0$; (v) closer to full compensation ($\eta=0.1$), the DOS seems to display an upward inflection near $E=0$ and apparently does not drop to zero. Unfortunately, we are unable to resolve this region numerically with the desired accuracy. For instance, at higher dilutions $x=0.2$, we can still see the curve of $\eta=0.2$ dropping to zero near $E=0$.

Naturally that, for all the cases with $\eta \neq 0$, the existence of $N_v^A - N_v^B$ zero modes is guaranteed. As before, we inspected this by calculating the missing spectral weight in the bands and confirmed that it does agree with the fraction of uncompensated vacancies. Hence, the picture emerging from these results seems to suggest that, although the gap disappears for $\eta < 1$, the DOS still drops to zero at $E=0$ and might drop in a singular way as η approaches zero. If we separate the contributions of the zero modes to the global DOS from the contribution of the other states, the consequence of this would be that, in a compensated lattice ($\eta=0$), the DOS associated with the other states would seem to diverge as $E \to 0$, but would be zero precisely at $E=0$. Stated in another way, coming from high energies, we would see a decreasing DOS up to some typical energy $\epsilon \sim \sqrt{x}$, at which point it would turn upward. At very small energies, the DOS would seem to be diverging but, at some point arbitrarily close to $E=0$, it would drop precipitously down to zero. Unfortunately, at the moment the numerical calculations are not so accurate as to allow the confirmation or dismissal of such possibility. In fact, the peaks for $\eta=0.0$ are of the same magnitude of the ones found when the dilution is completely random across the two sublattices [Fig. 6(a)]. So, although the evidence is compelling toward the affirmative, these results are still inconclusive as to whether the zero modes disappear in a perfectly compensated diluted lattice or not.

C. Local impurities

Vacancies are local scatterers in the unitary limit. A vacancy can be thought as an extreme case of a local potential U when $U \to \infty$. In this context, we investigated the intermediate case characterized by a finite local potential. The Hamiltonian in this case changes from the pure tight binding in Eq. (1) to

$$H = U \sum_p c_p^\dagger c_p - t \sum_{\langle i,j \rangle} c_i^\dagger c_j - t' \sum_{\langle\langle i,j \rangle\rangle} c_i^\dagger c_j + \text{H.c.} \tag{26}$$

The first term represents the local potential of magnitude U at the impurity sites p. These impurity sites belong to the underlying honeycomb lattice but their space distribution is random. The concentration of impurities, $x=N_i/N$, is kept constant and we consider only the case with $t'=0$ in the sequel.

Physically, the model summarized in the Hamiltonian of Eq. (26) could describe the situation in which some of the carbon atoms are substituted by a different species. Another realistic circumstance has to do with the fact that a real graphene sheet is expected to have some molecules from the environment adsorbed onto its surface.[23] Consequently, even if the honeycomb lattice of the carbon atoms is not disrupted with foreign atoms, the presence of adsorbed particles can certainly induce a local potential at the sites where they couple to the carbon lattice.

Much of the details of this model can be understood from the local environment around a single impurity, in which case exact results and closed formulas are obtainable within a T-matrix approach.[37] Hence, we start by analyzing the single impurity problem in the honeycomb lattice by taking into account the full electronic dispersion and calculating the exact local Green's functions, which allow the identification of the main spectral changes introduced by the scattering potential. Within T matrix, the 2×2 electron Green's function is written as

$$\boldsymbol{G}_{r,r'} = \boldsymbol{G}^0_{r,r'} + \sum_{s,s'} \boldsymbol{G}^0_{r,s} \boldsymbol{T}_{s,s'} \boldsymbol{G}^0_{s',r'}. \tag{27}$$

In the Dyson-like expansion above $\boldsymbol{G}^0$ is the noninteracting Green's function whose matrix elements are denoted by $[\boldsymbol{G}^0]^{\alpha,\beta}_{r,r'}$ (subscripts superscripts refer to position and sublattice, respectively), and the T matrix, $\boldsymbol{T}$ is formally defined in terms of the scattering potential $\boldsymbol{V}$ by[37,38]

$$\boldsymbol{T}(E) = \frac{\boldsymbol{V}}{1 - \boldsymbol{G}^0 \boldsymbol{V}}. \tag{28}$$

Taking $\boldsymbol{V}^{\alpha\beta}_{r,r'} = U \delta_{r,r'} \delta_{r,0} \delta_{\alpha,\beta} \delta_{\alpha,0}$ for a potential localized only on site $r=0$ of sublattice A, the local Green's function on that site reads

$$G^{AA}_{00} = \frac{[G^0]^{AA}_{00}}{1 - U[G^0]^{AA}_{00}}. \tag{29}$$

The function $[G^0]^{AA}_{00}$ is simply related to the density of states *per carbon atom* in the absence of impurity, $\rho^0(E)$, through

$$[G^0(E)]^{AA}_{00} = F(E) - i\pi\rho^0(E). \tag{30}$$

The knowledge of $\rho^0(E)$ suffices for the determination of $F(E)$ on account of the analytical properties of $\boldsymbol{G}^0(E)$ and the Kramers–Kronig relations. Moreover, any new poles of the exact Green's function can come only from the denominator in Eq. (29) and are determined by the condition

$$1 - UF(E) = 0. \tag{31}$$

Should this condition be satisfied for E within the branch cut of $\boldsymbol{G}^0$, the new poles will signal the existence of resonant states in the band, and bound states of the local potential otherwise. Since $\rho^0(E)$ is known exactly[39] (cf., Fig. 3), so is $\boldsymbol{G}^0(E)$ through Eq. (30). The function $F(E)$ is shown in Fig. 10. The profile of this function and the condition above allow two immediate conclusions without further calculation: (i) the presence of the local potential induces bound states beyond the band continuum and (ii) a resonance appears at low energies beyond a certain threshold U_{res} with energy of op-

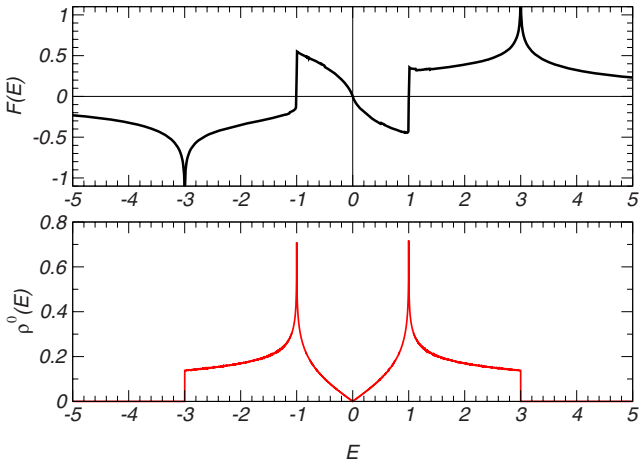

FIG. 10. (Color online) Real part of Eq. (30) (top) obtained from the homogeneous DOS (bottom) through the Kramers–Kronig relations.

posite sign with respect to the scattering potential, and which moves toward $E=0$ as $U\to\infty$.

The latter characteristic is certainly more interesting and we explore it a little further. To that extent, notice that from Eqs. (29) and (30) follows the interacting LDOS at the impurity site,

$$\rho_0(E) = \frac{\rho^0(E)}{[(1-UF(E)\ ]^2 + [\,\pi U\rho^0(E)]^2}. \tag{32}$$

This quantity was calculated using the results of Fig. 10 and Eq. (32) and, at the same time, using the recursive method that we have been using so far. The two do coincide, just as expected since the solution of the single impurity problem is exact, and on the other hand, the recursive method is exact for the particular case of the LDOS.[28] The LDOS at the site of the impurity is shown in the top frame of Fig. 11 for several values of U. The bottom frame shows the same data divided by the noninteracting DOS, which amounts to replacing $\rho^0(E)$ by unity in the numerator of Eq. (32). The resonance alluded above is visible in both panels through the

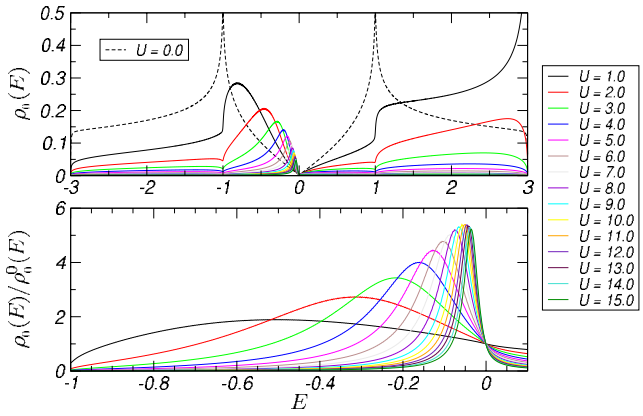

FIG. 11. (Color online) (Top) LDOS at the impurity site $[\rho_0(E)]$ for different strengths of the scattering potential, as indicated in the legend. (Bottom) The same data divided by the free DOS $[\rho^0(E)]$.

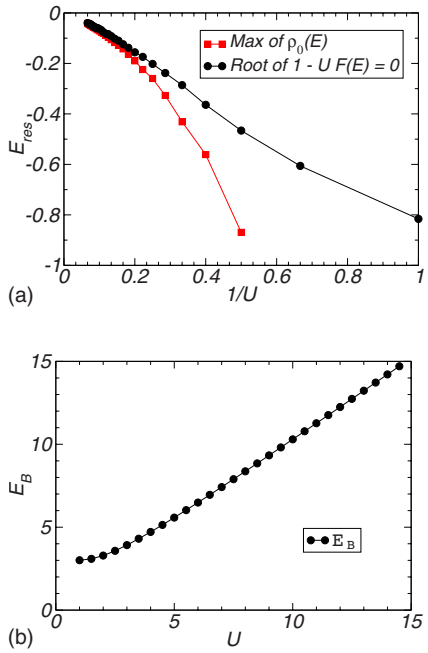

FIG. 12. (Color online) (a) Position of the maximum in the LDOS compared with the roots of Eq. (31). (b) Energy of the bound state.

marked enhancement of the LDOS in the vicinity of the Dirac point. The position of the maximum in $\rho_0(E)$ differs slightly from the roots of Eq. (31) due to the modulation introduced by $\rho^0(E)$ in Eq. (32). This effect is shown in detail in Fig. 12(a) where the two values are explicitly compared. In addition, the LDOS also exhibits the Dirac-delta peak associated with the bound state (not shown in the figure), whose energy is plotted in Fig. 12(b) as a function of U. It is worth mentioning that analytical expressions can be obtained for the resonant condition [Eq. (31)] using the low-energy Dirac approximation to the electronic dispersion.[31,36]

Returning now to our initial goal of populating the lattice with a finite concentration of local impurities, we expect the main features of the above analysis to hold to a large extent. However, new features should also emerge from the possibility of multiple scattering and interference effects in a multi-impurity environment. Although some of these effects can be captured within standard approximations to impurity problems,[38] we choose to present the exact numerical results obtained with the recursion technique. Examples of such calculations are shown in Fig. 13, where the global DOS averaged over several configurations of disorder is shown for different potential strengths and concentrations.

The presence of the local term clearly destroys the particle-hole symmetry, leading to the asymmetric curves in the figure. As Fig. 13(a) makes clear, among the features seen locally for a single impurity (Fig. 11), the ones that carry to the global DOS of the thermodynamic system with a finite concentration of impurities are the resonant enhancement of the DOS in the vicinity of the Dirac point, and the high energy features that dominate beyond the band edge, and are associated with the impurity states. One verifies that a finite concentration x generates a sort of impurity band at scales of the order of U, in accordance with the results in

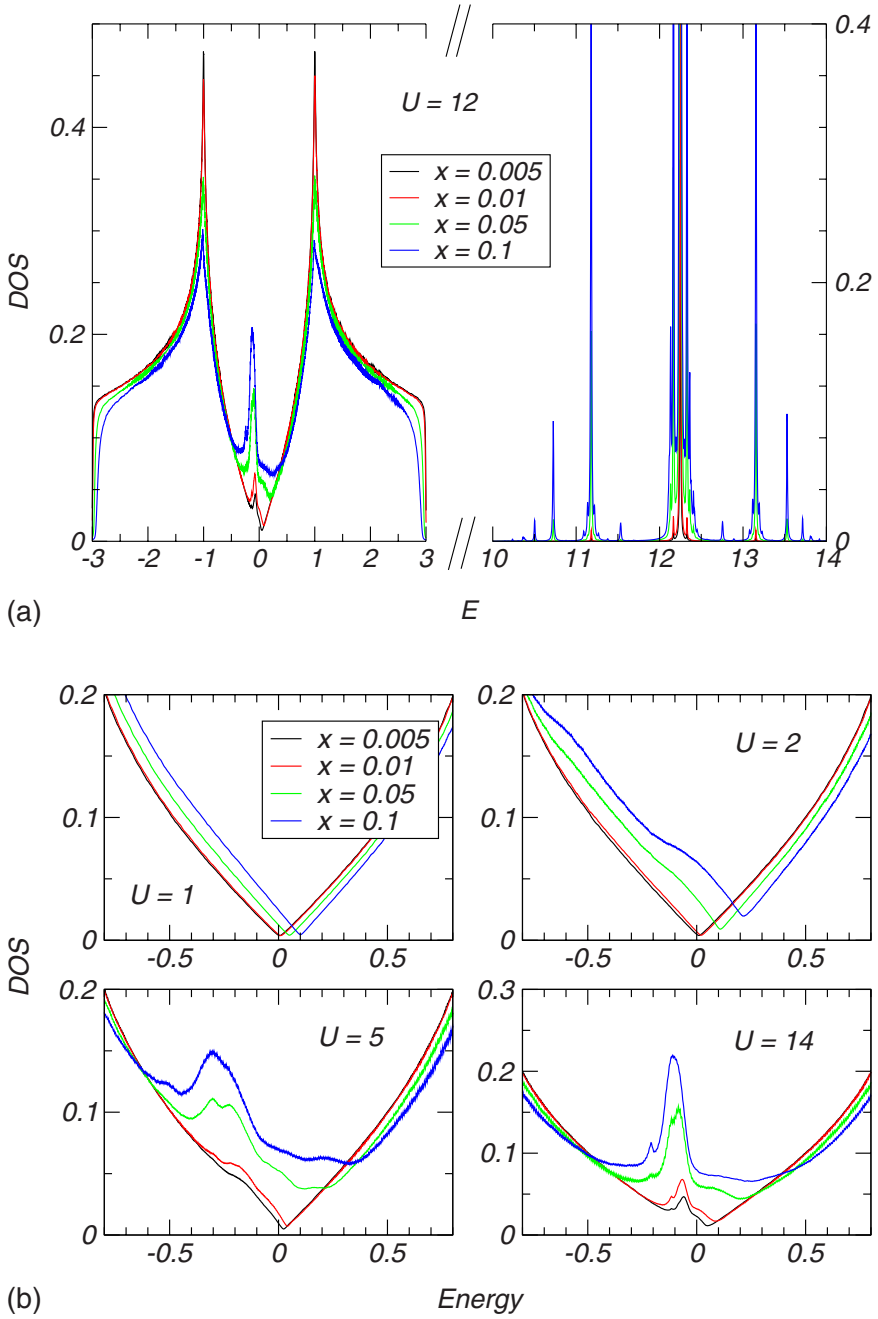

FIG. 13. (Color online) DOS of the honeycomb lattice with a finite density of local impurities. (a) shows the DOS for $U=12t$ and different concentrations of impurities (notice the truncation in the horizontal axis). (b) shows a detail of the low-energy region for different U and x as noted in the different graphs.

Fig. 12(b). This impurity band has an interesting splitted structure as can be seen in the figure and is completely detached from the main band for $U \gtrsim 4t$. In Fig. 13(b), we amplify the low-energy region and display what happens as U and x vary. At small x and U, the DOS changes only through a simple translation of the band with the concomitant shift in the Dirac point E_D [see the panel in Fig. 13(b) corresponding to $U=1$]. This rigid shift of the band at low disorder is simply a consequence of the rigid band theorem:[40] It states that the form of the DOS in an alloy system does not change with alloying, other than via a simple translation as given by first-order perturbation theory. In our case, the magnitude of this shift is given by

$$\Delta E = \left\langle U \sum_p c_p^\dagger c_p \right\rangle \simeq xU, \tag{33}$$

where an average over disorder is implied. We can confirm that the exact numerical results satisfy quantitatively this expectation by inspection of the data in Fig. 14(a). There, we plot the position of the minimum in the DOS E_D for several U and x, being evident that, for the concentrations analyzed, relation (33) is quite accurately satisfied up to $U \simeq 3$. For local potentials higher than $U \simeq 3$, the rigid shift of E_D

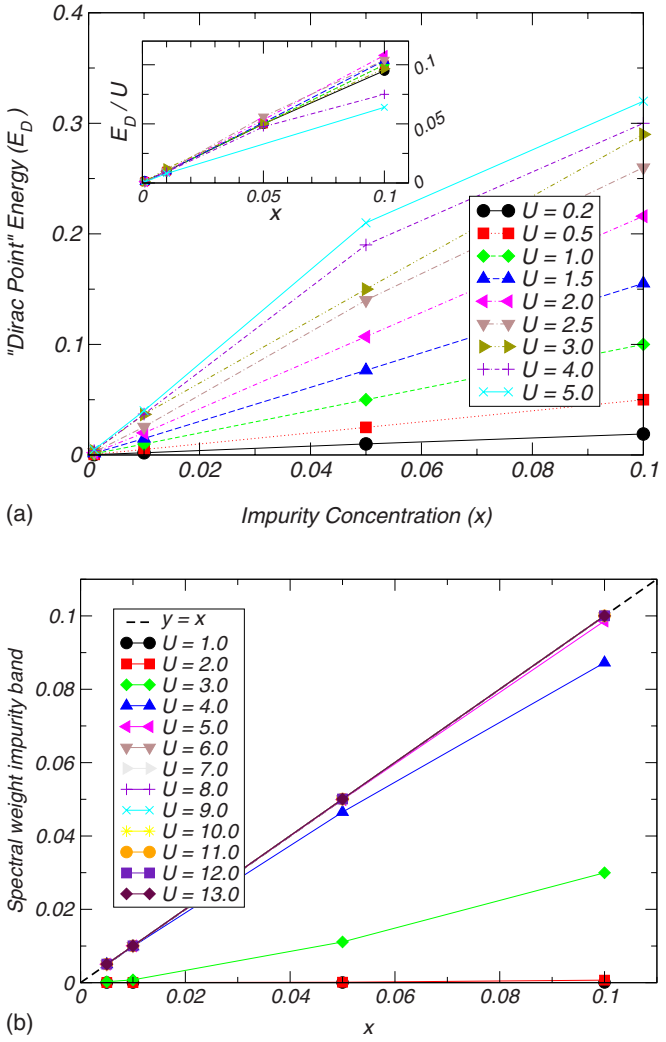

FIG. 14. (Color online) (a) Variation of the *Dirac point* energy E_D with impurity concentration and strength. The inset shows E_D/EU as a function of U, in which the curves with $U \leqslant 3$ roughly collapse onto each other. (b) Spectral weight transfer to the impurity band in the presence of local impurities. The values shown correspond to integration of the global DOS beyond $E=4t$ (above the main band edge, cf., Fig. 13).

breaks down and, in fact, the position of E_D becomes slightly ill defined.

We point out that, concurrently with the shift of E_D (and the band), there is a marked increase in the DOS at E_D and, unlike the single impurity case (cf., Fig. 11), the DOS becomes finite at E_D with increasing concentration. For potentials up to around $U=3-4$, although relation (33) still holds for the minimum in the DOS, the DOS starts to exhibit a characteristic bulge near $E=0$ on the valence band for a repulsive potential (see the second panel in Fig. 13), signaling the presence of the resonant states, which for these potentials are not yet clearly resolved in the spectral density. In fact, our data point to the existence of a critical potential strength $U \sim 1$ beyond which the resonant effects set in. Such critical potential has been recently addressed analytically in Ref. 41, where it appears as marking the onset of the so-called spectrum rearrangement regime.

Nonetheless, whereas E_D shifts linearly for moderate potential strengths, the position of the resonance does not vary significantly with concentration and is only enhanced with an increasing number of impurities [Fig. 13(b)].

Another noteworthy aspect of this model has to do with the impurity band that emerges at high energies. Besides the effects just described, a change in the concentration of impurities implies a concomitant redistribution of spectral weight between the main band and the impurity band. This is plainly shown in Fig. 14(b) which displays the spectral weight in the impurity band against the concentration of impurities. This spectral weight is calculated by integrating the DOS in the region $[4t,\infty[$. As the figure shows, for $U \gtrsim 5t$, the spectral weight of the impurity band saturates at the value x. This is seen from the fact that, when $U \gtrsim 5t$, the curves collapse onto a single line with unit slope (the auxiliary dashed line in the figure), signaling the detachment of the impurity states from the main band. For those cases, the spectral weight coincides with the concentration x. It certainly had to be so because with increasing U the impurity band drifts to higher energies, eventually disappearing from the problem in the unitary limit. As discussed previously in Sec. III A, the spectral weight of the main band is decreased by precisely x, in the presence of a concentration of vacancies of x. This is totally consistent with the fact that the local impurity interpolates between the clean case and the vacancy limit.

Finally, is also clear how the vacancy limit $(U \to \infty)$ emerges from the data in Fig. 13 as the resonance approaches $E=0$ and becomes more sharply defined. At the same time, the impurity band is displaced toward higher and higher energies, eventually projecting out of the problem in the vacancy limit.

D. Nondiagonal impurities

Another effect expected with the inclusion of a substitutional impurity in the graphene lattice is the modification of the hoppings between the new atom and the neighboring carbons. This happens because the host and substituting atoms have different radii because the nature of the orbitals involved in the conduction band is different or, most likely, a combination of both. Customary impurities in carbon allotropes are nitrogen, working as a donor, and boron, working as an acceptor.[42] In fact, the selective inclusion of nitrogen and/or boron impurities in carbon nanotubes is a current practice in the hope to tune the nanotubes' electronic response.[43–45]

In general, the study of a perturbation in the hopping is much less studied in problems with impurities than the case of diagonal, on-site perturbations. In the context of our investigations, the perturbation in the hopping can, again, be interpreted as an interpolation between a vacancy and an impurity. To be more precise, let us introduce the relevant Hamiltonian,

$$H = -t\sum_{i,\delta} c_i^\dagger c_{i+\delta} + t_0 {\sum_{p,\delta}}' c_p^\dagger c_{p+\delta} + \text{H.c.} \tag{34}$$

In this case, only the nearest-neighbor hopping is considered. Without the second term, H above is the Hamiltonian for

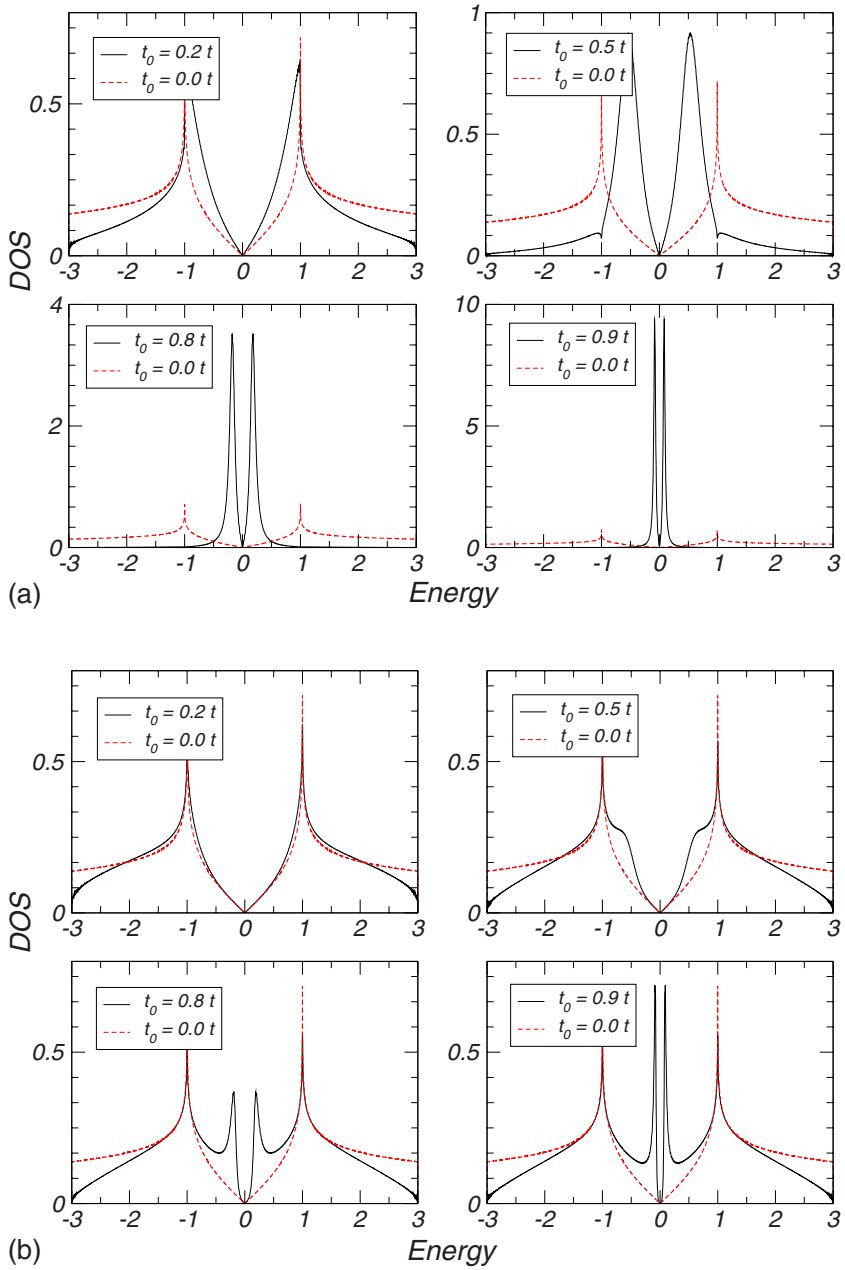

FIG. 15. (Color online) Effect of a single substitutional impurity in the LDOS. In panel (a), we plot the LDOS calculated at the site of the impurity for the four different values of t_0 indicated in each frame. In panel (b), the situation is identical but the LDOS is calculated at the nearest-neighboring site of the impurity.

pure graphene. The last sum is restricted to the impurity sites p and t_0 represents a perturbation in the hopping amplitude to its neighbors. Is plain to see that, when $t_0=t$, all the impurity sites turn into vacancies since the hopping thereto is zero. As a result of that, this model provides another type of interpolation between pure graphene and diluted graphene. An important difference is that this model can be disordered when the impurities are placed at random, without breaking particle-hole symmetry and, in this sense, is qualitatively much different from the case of local disorder discussed in the preceding section.

We first look at the LDOS in Fig. 15, which contains typical results for the local DOS near the impurity, and at the impurity site itself. Irrespective of whether the LDOS is calculated at or near the impurity, the resulting curves display a strong resonance in the low-energy region, no bound states are formed and the curves are symmetrical with respect to the origin. As t_0 increases from zero, two simultaneous modifications in these resonances take place. The first is that they are clearly enhanced as t_0 approaches t. The second is its shift in the direction of the Dirac point, in such a way that, when $t_0=0.9t$, the peak is already very close to $E=0$. With regard to this last point, we systematically investigated the variation of the peak position in the LDOS at the impurity site with the value of t_0. This dependence, which can be seen in Fig. 16, is approximately linear and, for $t_0 \gtrsim 0.6$, is rea-

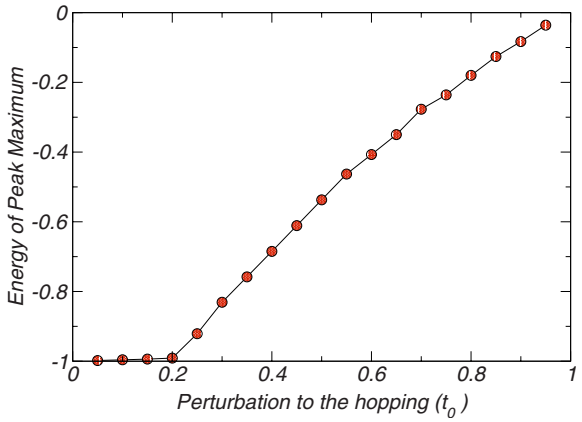

FIG. 16. (Color online) Variation of the energy corresponding to the peak in the LDOS with the magnitude of t_0. The LDOS in question is the LDOS calculated at the impurity site.

sonably well approximated by the linear function $\epsilon_{\max} \simeq t - t_0$. The apparent saturation for smaller t_0 is due to the proximity to the van Hove singularity. The study of a single substitutional impurity has been also undertaken in Ref. 46 with identical results.

The double-peak structure close to the Dirac point can be qualitatively understood from the results regarding a vacancy. Suppose that one completely severs the hopping between a given atomic orbital and its immediate neighbors (i.e., set $t_0=t$). In this case, we are left with an isolated orbital with energy $E=0$ and a vacancy in the honeycomb lattice, which we know also has a zero energy mode. If now t_0 is changed slightly, it will cause the hybridization of the two zero energy modes with the consequent splitting of the energy level, and hence the double peaked structure of the LDOS close to the Dirac point.

When we go from one impurity to a finite density of impurities x, we obtain a measurable influence in the thermodynamic limit. Our method in this case, consists in placing impurities at random positions in the lattice, keeping their concentration constant. The global DOS, averaged over several realizations of disorder, is presented in Fig. 17. For intermediate values of t_0, the perturbation in the hopping induces a resonance appearing at roughly the same energies, as the ones found in Fig. 16. The resonance is enhanced at higher concentrations of impurities and becomes more sharply defined as $t_0 \to t$. Interestingly, as can be seen in the last panels of Fig. 17 and its inset, the resonant peak splits at higher perturbations. This splitting depends on the concentration of impurities being more pronounced for larger concentrations and is a new feature introduced by the finite number of impurities. As happened already in the case of local impurities, the exact numerical results have qualitative and quantitative features that could not be anticipated from calculations with a single impurity within the usual approximation methods. We would also like to point out the fact that, from inspection of the above figures, the DOS remains zero at $E=0$, notwithstanding the sharp resonances in its vicinity. Since this model of disorder interpolates between clean graphene and graphene with vacancies, we are led to a situation similar to the one encountered in Sec. III B for uncompensated vacancies. As before, it seems that, as the vacancy limit is approached, the DOS remains zero at the Fermi energy, despite diverging arbitrarily close to this point, and so the question of the DOS exactly at $E=0$ for vacancies lingers. Furthermore, unlike what happens with local impurities, there is no impurity band nor any high energy features appearing as $t_0 \to t$: The action is all on the low energy regions. Strictly speaking, in the limit $t_0=t$, the impurity sites become isolated from the carbon network. Hence, those sites have to be removed from the Hilbert space for a meaningful physical description of the vacancy case as the limit $t_0 \to t$ (for local impurities the removal of the impurity sites is akin to the drift of the impurity band to infinity, carrying the spec-

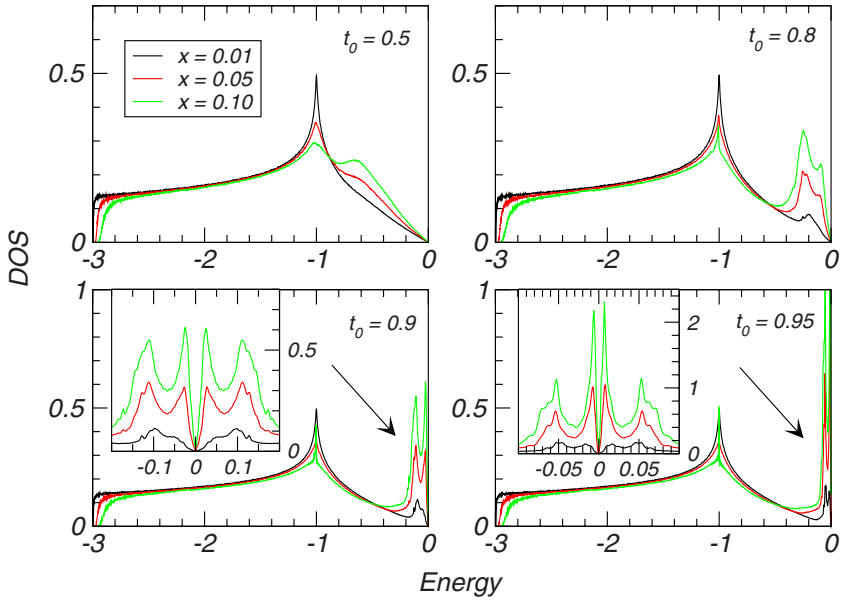

FIG. 17. (Color online) The DOS corresponding to the model Hamiltonian (34), with a finite density of impurities. The three panels correspond to different values of the perturbing hopping (t_0=0.5, 0.8, 0.9, and 0.95), and within each panel the three curves were obtained at different concentrations (x=0.01, 0.05, and 0.1). The inset of the bottom panels is a magnification of the region near E=0.

tral weight associated with the number of the impurities, which projects out of the problem).

Before closing, just a comment on the physical origin of this perturbation. In effect, the presence of a substitutional impurity like N or B will introduce, simultaneously, a perturbation in the hopping and in the local energy. However, it is more or less clear from the discussions in the previous section that the clearest resonances near E_F occur when the local potential U is moderate or high, which is not the case for boron or nitrogen substituents. For example, in Ref. 47, the local potential associated with such impurities is $U \sim t$, which, from the results above [e.g., Fig. 13(b)], means that their signature in the spectral density should be rather feeble or absent. On the other hand, a perturbation in the hopping of the order of $0.5t$ should already cause a significant increase in the Fermi velocity at $E=0$. Hence, when both are of the same order of magnitude as the hopping t, the perturbation in the hopping should be more significant in dictating the changes in the low-energy electronic structure in the real physical system.

IV. CONCLUSIONS

In this paper, we have studied the influence of local disorder in the electronic structure of graphene, within the tight-binding approximation of Eq. (1). We focused on vacancies in an otherwise perfect graphene plane and the not so extreme cases of local (diagonal) impurities and substitutional (nondiagonal or both) impurities. In all cases, we saw that disorder brings dramatic alterations of the spectrum in the vicinity of the Fermi level. This is highly significant since many of the peculiar physical properties of graphene stem from the vanishing of the DOS at the Dirac point.

In the case of vacancies, the DOS features a strong divergence at and close to $E=0$, which is associated with the formation of quasilocalized states decaying as $\sim 1/r$ around the vacancies, which remain even in the presence of next-nearest-neighbor hopping. Rather interesting is the particular case of lattices with uncompensated vacancies, in which case we found the appearance of a gap at low energies proportional to the concentration x, and the coexistence of localized zero modes in the middle of this gap. For the extreme limit of dilution among sites of a given sublattice only, we showed that the gap is robust, and that a macroscopic number of quasilocalized zero modes dominates the spectral density in the middle of the gap. Moreover, these zero modes are strictly nondispersive as imposed by symmetry and give a contribution $x\delta(E)$ to the gapped DOS. This is very interesting, in particular, if one reasons in terms of magnetic instabilities and formation of local magnetic moments. Such states might be at the origin of local magnetic moments, which would explain the magnetism seen experimentally in the irradiation experiments.[21,22] In effect, *ab initio* calculations agree in this respect[48,49]—for example, Ref. 48 shows the stabilization of local moments of $\simeq 1.5\mu_B$ per vacancy, opening the possibility for above room temperature magnetism—although the nature of the coupling between these moments and the explanation of such high T_C is still a matter of debate.[50,51]

We showed how the vacancy case emerges as the limiting case of a local impurity. In this case, the exact calculation with a single impurity problem was presented by taking into account the full dispersion of the honeycomb lattice. The results of approximate methods such as CPA were subsequently compared with the exact numerical solution of the problem with finite concentrations of impurities, and we identified the values of the parameters for which these approximations qualitatively break down (see also Ref. 41 for a discussion of the validity of CPA). The discussion of nondiagonal impurities provided yet another alternative view of the interpolation between clean graphene and vacancies, with relevance for systems with dopants that replace the host carbon atoms in the honeycomb lattice. One important aspect of the results with a finite concentration of these impurities regards the splitting of the low-energy peaks (insets of Fig. 17), which is not captured at a single particle level. The effect has to do with situations in which substitutional impurities appear close to each other, causing interference and hybridization effects that lead to the resplitting of the low-energy resonances. In both cases, the changes observed in the DOS close to the Dirac point within our tight-binding approach agree with *ab initio* calculations using different types of defects and/or impurities.[52,53]

Finally, the results provided for the DOS and LDOS are directly testable in real-life samples through scanning tunneling spectroscopy techniques and, moreover, the effects on the global DOS should reflect themselves in the electric transport. For example, one might be able to distinguish whether the main effect of a substitutional impurity occurs through the modification of the hopping to its neighbors or through the introduction of a local potential.

Note added. While preparing this manuscript we became aware of Ref. 54 with some overlapping results regarding local impurities.

ACKNOWLEDGMENTS

We acknowledge many motivating and fruitful discussions with N. M. R. Peres and F. Guinea. V.M.P. is supported by Fundação para a Ciência e a Tecnologia via SFRH/BPD/27182/2006. V.M.P. and J.M.B.L.d.S. further acknowledge POCI 2010 via the grant PTDC/FIS/64404/2006. A.H.C.N. was supported through the NSF grant DMR-0343790.

[1] A. K. Geim and K. Novoselov, Nat. Mater. **6**, 183 (2007).
[2] A. H. Castro Neto, F. Guinea, and N. M. R. Peres, Phys. World **19**, 33 (2006).
[3] A. H. Castro Neto, F. Guinea, N. M. R. Peres, K. S. Novoselov, and A. K. Geim, arXiv:0709.1163 (unpublished).
[4] K. S. Novoselov, A. K. Geim, S. V. Morozov, D. Jiang, Y. Zhang, S. V. Dubonos, I. V. Grigorieva, and A. A. Firsov, Science **306**, 666 (2004).
[5] R. Chang, *Chemistry*, 4th ed. (McGraw Hill, New York, 1991).
[6] K. S. Novoselov, D. Jiang, F. Schedin, T. J. Booth, V. V. Khotkevich, S. V. Morozov, and A. K. Geim, Proc. Natl. Acad. Sci. U.S.A. **102**, 10453 (2005).
[7] P. R. Wallace, Phys. Rev. **71**, 622 (1949).
[8] G. W. Semenoff, Phys. Rev. Lett. **53**, 2449 (1984).
[9] K. S. Novoselov, A. K. Geim, S. V. Morozov, D. Jiang, M. I. Katsnelson, I. V. Grigorieva, S. V. Dubonos, and A. A. Firsov, Nature (London) **438**, 197 (2005).
[10] M. I. Katsnelson and K. S. Novoselov, Solid State Commun. **143**, 3 (2007).
[11] V. M. Pereira, J. Nilsson, and A. H. Castro Neto, Phys. Rev. Lett. **99**, 166802 (2007).
[12] A. V. Shytov, M. I. Katsnelson, and L. S. Levitov, Phys. Rev. Lett. **99**, 246802 (2007).
[13] N. M. R. Peres, A. H. Castro Neto, and F. Guinea, Phys. Rev. B **73**, 241403(R) (2006).
[14] F. Miao, S. Wijeratne, Y. Zhang, U. C. Coskun, W. Bao, and C. N. Lau, Science **317**, 1530 (2007).
[15] C. Beenakker, A. Akhmerov, P. Recher, and J. Tworzydlo, Phys. Rev. B **77**, 075409 (2007).
[16] V. V. Cheianov, V. Fal'ko, and B. L. Altshuler, Science **315**, 1252 (2007).
[17] T. Ando and T. Nakanishi, J. Phys. Soc. Jpn. **67**, 1704 (1998).
[18] C. L. Kane and E. J. Mele, Phys. Rev. Lett. **95**, 226801 (2005).
[19] S. Cho, Y.-F. Chen, and M. S. Fuhrer, Appl. Phys. Lett. **91**, 123105 (2007).
[20] A. Rycerz, J. Tworzydlo, and C. W. J. Beenakker, Nat. Phys. **3**, 172 (2007).
[21] P. Esquinazi, D. Spemann, R. Höhne, A. Setzer, K.-H. Han, and T. Butz, Phys. Rev. Lett. **91**, 227201 (2003).
[22] J. Barzola-Quiquia, P. Esquinazi, M. Rothermel, D. Spemann, T. Butz, and N. Garcia, Phys. Rev. B **76**, 161403(R) (2007).
[23] F. Schedin, A. K. Geim, S. V. Morozov, D. Jiang, E. H. Hill, P. Blake, and K. S. Novoselov, Nat. Mater. **6**, 652 (2007).
[24] J. C. Meyer, A. K. Geim, M. I. Katsnelson, K. S. Novoselov, T. J. Booth, and S. Roth, Nature (London) **446**, 60 (2007).
[25] C. H. Lewenkopf, E. R. Mucciolo, and A. H. Castro Neto, Phys. Rev. B **77**, 081410(R) (2008).
[26] V. M. Pereira, F. Guinea, J. M. B. Lopes dos Santos, N. M. R. Peres, and A. H. Castro Neto, Phys. Rev. Lett. **96**, 036801 (2006).
[27] V. M. Pereira, Ph.D. thesis, Universidade do Porto, 2006.
[28] R. Haydock, V. Heine, and M. J. Kelly, J. Phys. C **5**, 2845 (1972).
[29] R. Haydock, V. Heine, and M. J. Kelly, J. Phys. C **8**, 2591 (1975).
[30] J. González, F. Guinea, and M. A. H. Vozmediano, Phys. Rev. Lett. **69**, 172 (1992).
[31] N. M. R. Peres, F. Guinea, and A. H. Castro Neto, Phys. Rev. B **73**, 125411 (2006).
[32] N. D. Mermin and H. Wagner, Phys. Rev. Lett. **17**, 1133 (1966).
[33] P. C. Hohenberg, Phys. Rev. **158**, 383 (1967).
[34] F. Ding, Phys. Rev. B **72**, 245409 (2005).
[35] P. W. Brouwer, E. Racine, A. Furusaki, Y. Hatsugai, Y. Morita, and C. Mudry, Phys. Rev. B **66**, 014204 (2002).
[36] Y. V. Skrypnyk and V. M. Loktev, Phys. Rev. B **73**, 241402(R) (2006).
[37] R. J. Elliot, J. A. Krumhansl, and P. L. Leath, Rev. Mod. Phys. **46**, 465 (1974).
[38] S. Doniach and E. H. Sondheimer, *Green's Functions for Solid State Physicists* (Imperial College, London, 1999).
[39] T. Hanisch, B. Kleine, A. Ritzl, and E. Mueller-Hartmann, Ann. Phys. (N.Y.) **507**, 303 (1995).
[40] C. Kittel, *Quantum Theory of Solids* (Wiley, New York, 1963).
[41] Y. V. Skrypnyk and V. M. Loktev, Low Temp. Phys. **33**, 762 (2007).
[42] W. Kaiser and W. L. Bond, Phys. Rev. **115**, 857 (1959).
[43] R. Droppa, C. T. M. Ribeiro, A. R. Zanatta, M. C. dos Santos, and F. Alvarez, Phys. Rev. B **69**, 045405 (2004).
[44] S. Ciraci, S. Dag, T. Yildirim, O. Gülseren, and R. T. Senger, J. Phys.: Condens. Matter **16**, R901 (2004).
[45] A. H. Nevidomskyy, G. Csányi, and M. C. Payne, Phys. Rev. Lett. **91**, 105502 (2003).
[46] N. M. R. Peres, F. D. Klironomos, S.-W. Tsai, J. R. Santos, J. M. B. L. dos Santos, and A. H. Castro Neto, Europhys. Lett. **80**, 67007 (2007).
[47] Y. G. Pogorelov, arXiv:cond-mat/0603327 (unpublished).
[48] O. V. Yazyev and L. Helm, Phys. Rev. B **75**, 125408 (2007).
[49] L. Pisani, B. Montanari, and N. M. Harrison, arXiv:0710.0957 (unpublished).
[50] M. A. H. Vozmediano, M. P. López-Sancho, T. Stauber, and F. Guinea, Phys. Rev. B **72**, 155121 (2005).
[51] S. Saremi, Phys. Rev. B **76**, 184430 (2007).
[52] E. J. Duplock, M. Scheffler, and P. J. D. Lindan, Phys. Rev. Lett. **92**, 225502 (2004).
[53] M. W. C. Dharma-Wardana, Phys. Rev. B **75**, 075427 (2007).
[54] S. Wu, L. Jing, Q. Li, Q. W. Shi, J. Chen, X. Wang, and J. Yang, arXiv:0711.1018 (unpublished).